Contents lists available at ScienceDirect

Transactions of Nonferrous Metals Society of China

36(2026) 112−123

www.tnmsc.cn

Effect of different artificial aging treatments on tensile creep behavior of extruded lean Mg−Al−Ca−Mn alloy

Ming-yu LI [a], Zhi-ping GUAN [a,*], Jia-wang SONG [a,**], Hong-jie JIA [a], Pin-kui MA [a], Gang WANG [b], Wei YAN [b], Ming-hui WANG [a], Zhi-gang LI [a]

[a] Key Laboratory of Automobile Materials, Ministry of Education, School of Materials Science and Engineering, Jilin University, Changchun 130022, China;

[b] FAW Tooling Die Manufacturing Co., Ltd., Changchun 130000, China

Abstract: The effects of artificial aging (T6) on the creep resistance with tensile stresses in the range of 50−80 MPa at 175 °C were investigated for an extruded Mg−1.22Al−0.31Ca−0.44Mn (wt.%) alloy. The Guinier-Preston (G.P.) zones primarily precipitate in the sample aged at 200 °C for 1 h (T6-200°C/1h), while the Al_2Ca phases mainly precipitate in the sample aged at 275 °C for 8 h (T6-275°C/8h). The T6-200°C/1h sample exhibits excellent creep resistance, with a steady-state creep rate one order of magnitude lower than that of the T6-275°C/8h sample. The abnormally high stress exponent (~8.2) observed in the T6-200°C/1h sample is associated with the power-law breakdown mechanism. TEM analysis illuminates that the creep mechanism for the T6-200°C/1h sample is cross-slip between basal and prismatic dislocations, while the T6-275°C/8h sample exhibits a mixed mechanism of dislocation cross-slip and climb. Compared with the Al_2Ca phase, the dense G.P. zones effectively impede dislocation climb and glide during the creep process, demonstrating superior creep resistance of the T6-200°C/1h sample.

Keywords: Mg−Al−Ca−Mn alloy; tensile creep; artificial aging; cross slip

1 Introduction

The magnesium (Mg) alloys have gained considerable interest in response to the increasing need for lightweight materials in the transportation and aerospace industries. This is primarily because of their favorable specific strength and low density [1−3]. However, poor creep performance limits their high-temperature applications [4,5]. In recent years, research has focused mainly on enhancing the creep resistance of Mg-based alloys by adding rare-earth (RE) elements [6−8]. Many Mg−RE alloys with excellent creep performance have been developed, most of which involve Mg−Gd and Mg−Y based alloys. However, the addition of RE elements increases the cost of alloys, making them unsuitable for widespread commercial applications. Therefore, the development of low-cost, heat-resistant Mg alloys is crucial. Among non-RE Mg alloys, the Mg−Al−Ca−Mn alloy system has gained widespread attention owing to its excellent creep resistance and cost-effectiveness [9−11].

Creep is a critical consideration in engineering applications in which components are subjected to prolonged mechanical stress at elevated temperatures. The principal creep mechanisms include atomic diffusion, dislocation glide, and climbing [12−15]. The evolution of the micro-structure in Mg−Al−Ca−Mn alloys during the creep,

Corresponding author: *Zhi-ping GUAN, Tel: +86-13504464473, E-mail: guanzp@jlu.edu.cn;
**Jia-wang SONG, Tel: +86-13504314789, E-mail: songjw@jlu.edu.cn

https://doi.org/10.1016/S1003-6326(25)66952-4

Received 6 May 2024; accepted 17 January 2025

specifically the alterations in the precipitate morphology, distribution, and phase composition, significantly impacts their mechanical properties and resistance to creep. The addition of Ca can result in the formation of thermally stable intermetallic compounds, specifically, Mg_2Ca (C14) and Al_2Ca (C15) [16]. ZHU et al [17] studied squeeze-cast Mg−Al−Ca alloys and reported that the $(Mg,Al)_2Ca$ phases improve creep resistance. SUZUKI et al [18] reported that the Al_2Ca phase in a die-cast Mg−Al−Ca alloy poses a significant obstacle to non-basal dislocation slip. Moreover, artificial aging treatments exert a notable influence on the microstructural features of these alloys, consequently affecting their creep behavior. Single-layer ordered Guinier-Preston (G.P.) zones were observed in aged Mg−0.5Al−0.3Ca (wt.%) alloy [19] and Mg−3.6Al−3.4Ca−0.3Mn (wt.%) alloy [20]. HOMMA et al [21] demonstrated that the addition of Mn significantly enhances the creep resistance of Mg−6Al−3Ca (wt.%) alloys, and both the Al_2Ca phases and spherical precipitates (Al−Mn phases) improve the creep properties. Furthermore, dynamic precipitation in the G.P. zone also contributes to the creep resistance of the alloy.

The precipitates resulting from the artificial aging treatment may have a more complex impact on creep performance. AMBERGER et al [22] found that heat treatment did not significantly affect the creep performance of AZ91 alloy with the addition of 5 wt.% Ca. ZHANG et al [23] also observed that Mg alloys exhibited superior creep resistance after overaging. Although many studies have proposed various factors that affect the creep performance of Mg−Al−Ca−Mn alloys, there is still limited research on the effects of different aging conditions on creep performance. Because precipitates can be controlled by adjusting the aging conditions, it is essential to accurately identify the distinct influence of each type of precipitate on creep resistance. Hence, the Mg−1.22Al−0.31Ca−0.44Mn (AXM100) alloy was selected as the focus of this research to analyze the effects of the G.P. zones and precipitate phases on the creep properties through different aging treatments. This study aims to fill the existing research gap concerning the creep behavior of AXM100 alloy under different aging conditions and establish the relationship between aging treatments and creep properties. The findings of this study provide valuable insights into the development of cost-effective, novel, high-temperature, and creep-resistant magnesium alloys.

2 Experimental

The composition of the Mg−1.22Al−0.31Ca−0.44Mn (AXM100) alloy was determined using an optical spectrum analyzer (ARL 4460, Switzerland), and the results are presented in Table 1. Commercially pure Mg (99.90 wt.%) was first melted in an electric furnace at ~690 °C under a protective gas mixture of 99.5% CO_2 and 0.5% SF_6. Then, pure Al (99.90 wt.%), Mg−23.5Ca (wt.%), and Mg−3.5Mn (wt.%) were added into the Mg melt. The homogenization treatment process for the AXM100 alloy ingots included treatment at 300 °C for 3 h, followed by treatment at 420 °C for 8 h, and then at 450 °C for 4 h. The billets were subsequently extruded to form plates 40 mm wide and 5 mm thick at 390 °C, with an extrusion ratio of ~35∶1. The extruded sheets were subjected to solid-solution (T4) treatment at 500 °C for 0.5 h. Subsequently, the T4 samples were subjected to artificial aging (T6) at 200 and 275 °C.

Table 1 Composition of AXM100 alloy (wt.%)

Al	Ca	Mn	Fe	Si	Mg
1.22	0.31	0.44	<0.01	<0.02	Bal.

The gauge length of the tensile creep samples is 25 mm (along the extrusion direction), with a gauge width of 6.5 mm and thickness of 5 mm, as shown in Fig. 1. Tensile creep tests were conducted using an electronic creep test machine (RDL50) equipped with an environmental chamber capable of controlling the temperature to be within ±1 °C. The samples were heated to 175 °C, held for 20 min, and then pulled under four constant applied stresses of 50, 60, 70, and 80 MPa, respectively. The creep deformation within the gauge length of the sample was measured using two symmetrically arranged grating rulers with a precision of ±0.5 μm.

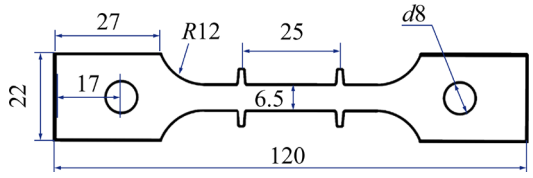

Fig. 1 Dimensions of tensile creep specimen (Unit: mm)

The Vickers microhardness of the alloy after the aging treatment was measured using a microhardness tester (HVS−1000A). The average hardness values were recorded based on at least ten measurements. Electrical conductivity was measured using a D60K digital test instrument. The microstructure was characterized using a scanning electron microscope (SEM, ZEISS Sigma 500) equipped with an EBSD (Oxford Instrument). The EBSD samples were electro-polished at 20 V for 90−120 s at −30 °C. The EBSD data were analyzed using AZtec and Channel 5.0. The precipitation behavior and dislocation characterization were observed using transmission electron microscopy (TEM, JEM−2100F). Circular test samples with a thickness of approximately 80 μm and diameter of approximately 3 mm were prepared for TEM observation. Subsequently, the samples were thinned using a precision ion thinning instrument (Gatan 691), and the temperature was maintained below −120 °C using liquid nitrogen.

3 Results

3.1 Initial microstructures

SEM backscattered electron (BSE) images illustrate the phases of the as-extruded and T4-treated AXM100 alloys. Surface scans conducted using energy-dispersive X-ray spectroscopy (EDS) reveal the presence of Al−Mn and small Al−Ca phases within the extruded sample. From Fig. 2(b), it is observed that after 0.5 h T4 treatment at 500 °C, nearly all the Al−Ca phases dissolve back into the Mg matrix, with the remaining phases primarily consisting of Al−Mn phases.

ZHANG et al [24] determined that the formation of G.P. zones was still evident after aging at T6 treatment (250 °C, 8 h). As a result, aging at 200 and 275 °C was selected to compare the effects of G.P. zones and Al_2Ca on the creep behavior. Figure 3(a) presents the Vickers hardness of the AXM100 alloy at various aging temperatures over time. The hardness decreases noticeably after T4 treatment. After heating at 200 °C for 1 h, a peak-aging hardness of ~HV 61 is reached, indicating a rapid aging response. The hardness remains relatively stable for 100 h. At 275 °C, a peak aging hardness of HV 53 is achieved at 0.5 h, which is lower than the peak hardness at 200 °C.

In terms of electrical conductivity, as depicted in Fig. 3(b), there is minimal variation in the electrical conductivity at 200 °C with increasing aging time. However, at 275 °C, the electrical conductivity continues to increase with increasing aging time. When the G.P. zones precipitate and remain stable, the electrical conductivity remains relatively constant. After aging at 275 °C, particles precipitate from the matrix and continue to grow. This reduction in supersaturated solute atoms results in a decrease in the lattice distortion of the matrix,

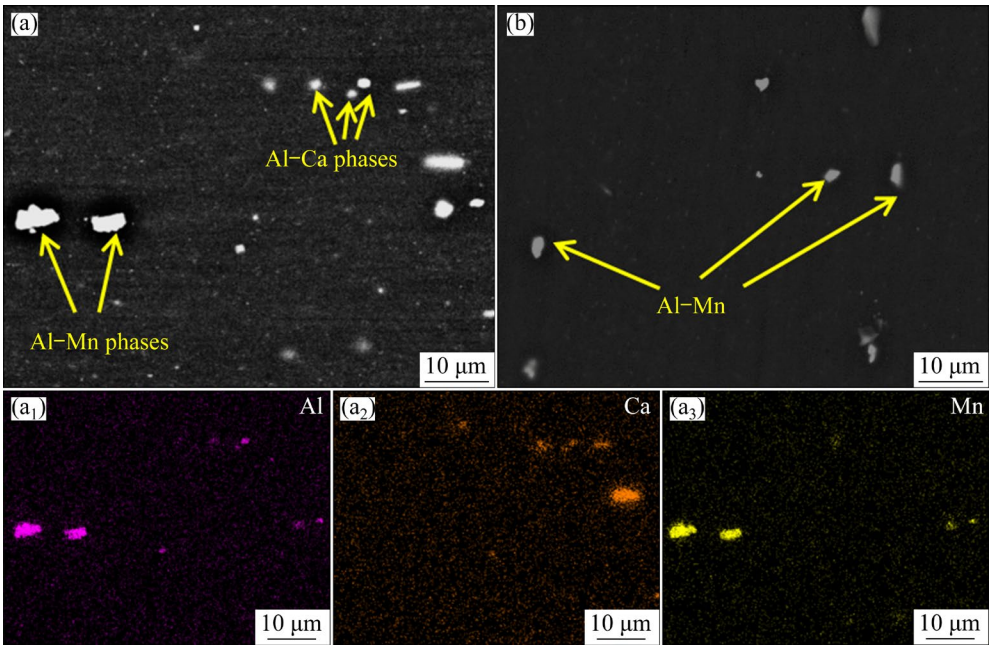

Fig. 2 SEM image and EDX mappings for extruded (a, a_1−a_3) and T4-treated (b) AXM100 alloy

leading to an increase in electrical conductivity [25,26]. The sample aged at 200 °C for 1 h is labeled as T6-200°C/1h, and the sample aged at 275 °C for 8 h is labeled as T6-275°C/8h. To investigate the influence of the G.P. zone and precipitates on the relative creep rates and rupture strains, T6-200°C/1h and T6-275°C/8h samples were chosen for further analysis.

TEM was employed to characterize the aging precipitates with different T6 treatments. Observations were made from the zone axes of $[10\bar{1}0]$ and $[\bar{2}110]$, as shown in Fig. 4. Figure 4(a) shows the presence of high dense G.P. zones through T6 (200 °C, 1 h) treatment, which are parallel to the $(0002)_{Mg}$ basal plane. The corresponding Fast Fourier Transform (FFT) pattern in Fig. 4(b) displays four distinct continuous stripes at the 1/3 and 2/3$\{11\bar{2}0\}$ positions (yellow arrows), indicating the presence of G.P. zones. The HRTEM image in Fig. 4(c) reveals that the G.P. zone, with a length of ~5 nm and a monatomic layer thickness of ~0.51 nm, exhibits a coherent interface with the Mg matrix. The observed characteristics of the G.P. zone align with those reported by OH-ISHI et al [27] and PING et al [28]. In Fig. 4(d), many Al_2Ca phases with an average length of ~60 nm and thickness of ~2.87 nm are dispersed along the $(0002)_{Mg}$ basal plane. The absence of stripes in Fig. 4(e) indicates

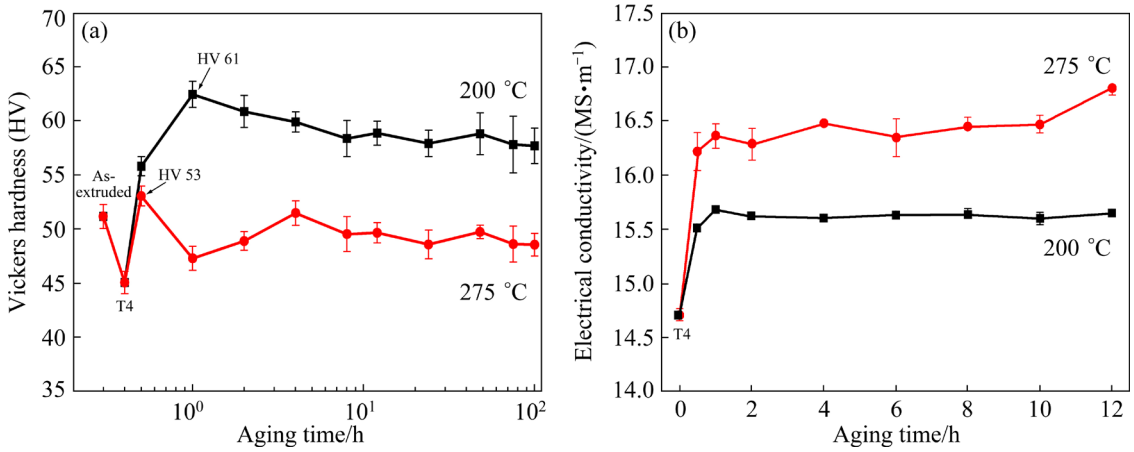

Fig. 3 Hardness (a) and electrical conductivity (b) changes of alloy aged at various temperatures

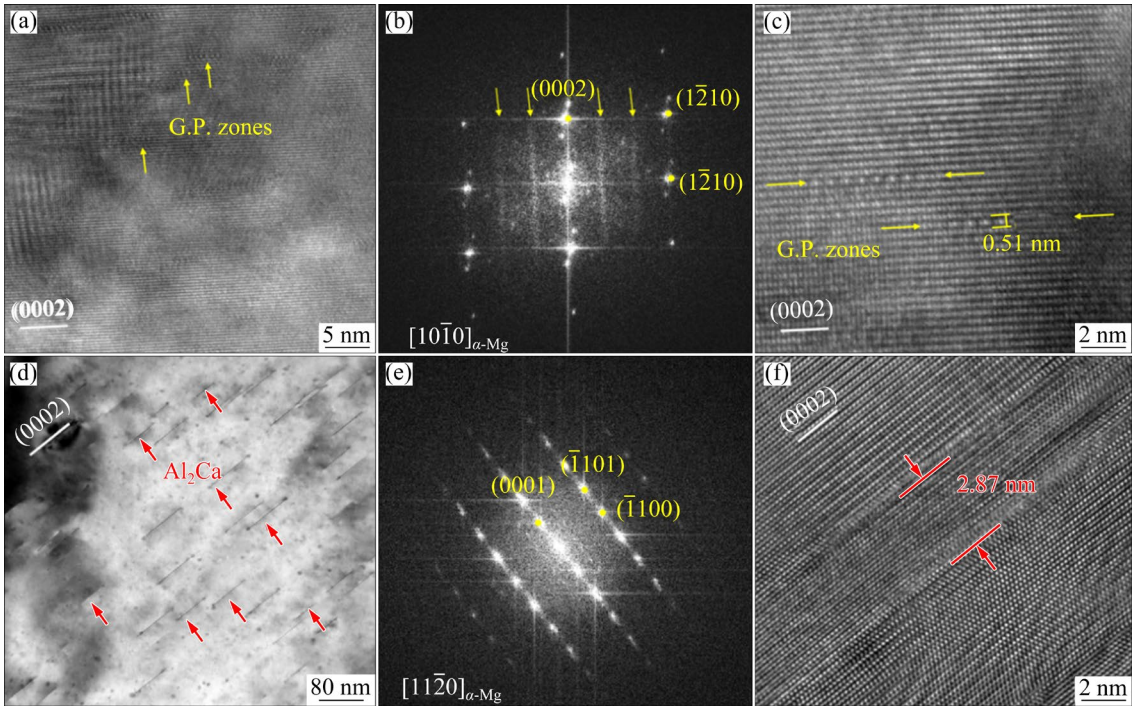

Fig. 4 Bright field (BF) TEM images (a, d), FFT patterns (b, e), and HRTEM images (c, f) of T6-200°C/1h (a−c) and T6-275°C/8h (d−f) samples

that the G.P. zones cannot maintain stability during T6 (275 ℃, 8 h) treatment.

Furthermore, EBSD analysis was performed on alloys subjected to two different aging treatments, as depicted in Fig. 5. It is evident that the alloy exhibits a typical fiber basal texture, with the *c*-axes of the majority of grains being perpendicular to the ED. The grain size of the T6-200°C/1h sample is approximately 54 μm, while that of the T6-275°C/8h sample is nearly 60 μm. Both aged samples display similar grain sizes and texture strengths, indicating that these factors do not influence the creep properties of the alloy.

3.2 Tensile creep properties

Figure 6 presents the creep strain versus time curves at 175 °C with tensile stresses in range of 50−80 MPa. The G.P. zones can be stably present at 175 °C, and a stress range of 50−80 MPa is also a common research scope for low-content non-rare earth Mg alloys [14]. Tables 2 and 3 present a summary of the steady-state creep rates and the corresponding creep strains over 50 and 100 h for AXM100 alloy under various conditions. As the stress increases, the steady-state creep rate increases. Under the same stress and temperature conditions, the T6-200°C/1h sample exhibits excellent creep resistance, with a steady-state creep rate one order of magnitude lower than that of the T6-275°C/8h sample. With the tensile stresses of 50 MPa, the creep strain over 100 h for the T6-275°C/8h sample is ~2.13%, almost ten times that of the T6-200°C/1h sample (~0.22%). The T6-275°C/8h samples with the tensile stresses of 70 and 80 MPa exhibit the third stage of creep with fractures occurring at 96 and 49 h, respectively. These results indicate that the creep resistance of the T6-200°C/1h samples is significantly superior to that of the T6-275°C/8h samples and that the presence of G.P. zones contributes to improving the creep resistance.

Furthermore, the creep resistance of the T6-200°C/1h sample exhibits certain advantages compared to commercial alloys such as AZ31, AZ61, and AZ91 [29]. CHEN et al [29] conducted tensile creep experiments on peak-aged AZ91 alloy and found that the steady-state creep rate with the tensile

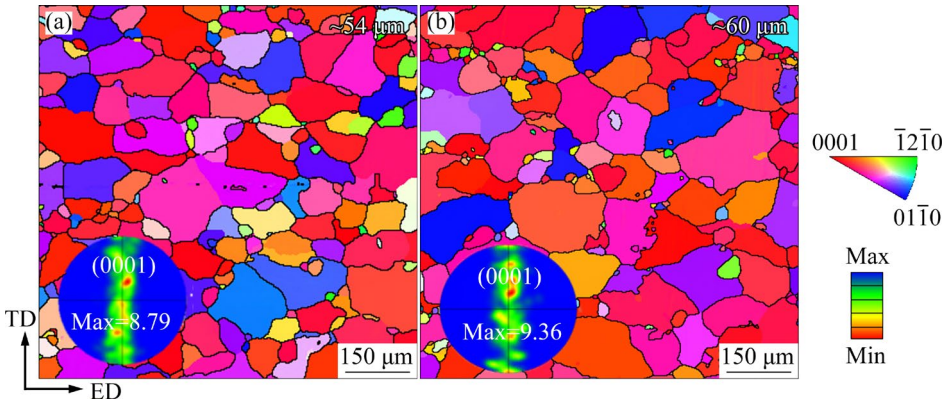

Fig. 5 Inverse pole figure of samples: (a) T6-200°C/1h; (b) T6-275°C/8h

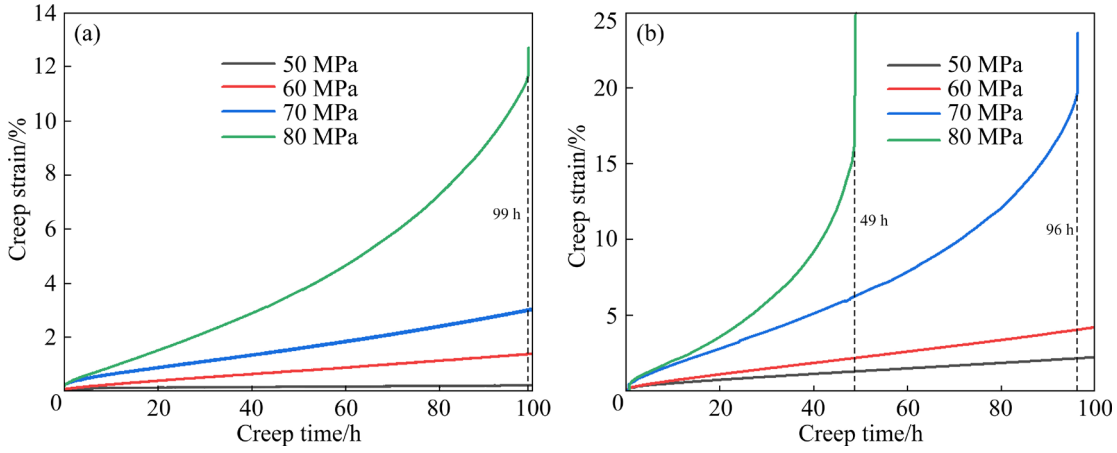

Fig. 6 Tensile creep curves of samples at 175 °C: (a) T6-200°C/1h; (b) T6-275°C/8h

Table 2 Creep data of T6-200℃/1h sample at 175 °C

σ/MPa	$\dot{\varepsilon}_m$ /s^{-1}	ε_{50h}/%	ε_{100h}/%	$\varepsilon_{fracture}$/%
50	3.08×10^{-9}	0.17	0.22	–
60	3.45×10^{-8}	0.76	1.39	–
70	6.51×10^{-8}	1.56	3.05	–
80	1.67×10^{-7}	3.69	–	11.70

Table 3 Creep data of T6-275℃/8h sample at 175 °C

σ/MPa	$\dot{\varepsilon}_m$ /s^{-1}	ε_{50h}/%	ε_{100h}/%	$\varepsilon_{fracture}$/%
50	5.30×10^{-8}	1.21	2.13	–
60	1.03×10^{-7}	2.09	4.08	–
70	3.19×10^{-7}	6.62	–	15.17
80	6.57×10^{-7}	–	–	19.74

stress of 70 MPa at 180 °C was ~1.50×10^{-7} s^{-1}. In contrast, the creep resistance of the T6-200°C/1h sample is more superior under similar stress and temperature conditions compared to the peak-aged AZ91 samples. Additionally, ZHANG et al [30] conducted creep experiments on a high-alloy content die-cast AXM90302 alloy at 150 °C and 70 MPa, where the alloy exhibited a steady-state creep rate of ~1.24×10^{-7} s^{-1} and a creep deformation of ~6.28% over 100 h. In comparison, the T6-200°C/1h sample, with its lower alloying content, demonstrates a steady-state creep rate nearly an order of magnitude lower under the same stress and temperature conditions. Creep strain over 100 h is only ~3.05%, indicating more superior creep resistance.

3.3 Creep stress exponent

The influence of stress and temperature on the steady-state creep rate ($\dot{\varepsilon}_m$) can be expressed using the power-law relationship [31]:

$$\dot{\varepsilon}_m = A\sigma^n \exp[-Q/(RT)] \quad (1)$$

where A is a constant that depends on the material, σ is the applied stress, n is the stress exponent, Q is the activation energy for creep, R is the molar gas constant and T is the thermodynamic temperature. A double logarithmic plot of the steady creep rates as a function of the applied stress at 175 °C is shown in Fig. 7. According to Eq. (1), the stress exponent n can be determined using the following equation [31]:

$$n=\left[\frac{\partial \ln \dot{\varepsilon}_m}{\partial \ln \sigma}\right]_T \quad (2)$$

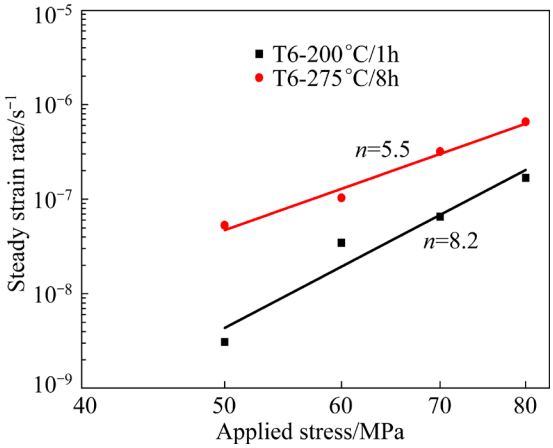

Fig. 7 Double-logarithmic plots of steady-state creep rate versus applied stress for T6-200℃/1h and T6-275℃/8h samples

The T6-200°C/1h and the T6-275°C/8h samples have the n values of ~8.2 and ~5.5, respectively. The value of n=1 corresponds to diffusion based creep; when n=2, grain boundary sliding plays a dominant role in controlling the rate. When n=3−7, dislocation movements (glide and/or climb) become the primary deformation mechanisms during the creep [32,33]. Hence, the creep behavior of the T6-275°C/8h samples is primarily governed by dislocation motion. When n>7 in the T6-200°C/1h sample, a power-law breakdown may occur. Therefore, further analysis is required to determine the stress exponent.

SHERBY and BURKE [34] proposed a criterion for material creep power-law breakdown. The conditions under which power-law breakdown occurs are as follows:

$$\dot{\varepsilon}/D > 10^{13}\text{m}^{-2} \quad (3)$$

D is the lattice diffusion coefficient for rate-controlled creep and satisfies the following relationship [35]:

$$D=D_0\exp[-Q_{sd}/(RT)] \quad (4)$$

where D_0 is 10^{-4} m^2/s, and Q_{sb} (lattice self-diffusion energy) is 135 kJ/mol [36]. The applied stress is normalized using the shear modulus, and the temperature dependence of the shear modulus of Mg can be determined by $\mu=1.92\times10^4-8.6T$ [37]. The steady-state creep rate normalized by the activation energy for the self-diffusion of Mg is plotted against the effective stress normalized by the shear modulus in Fig. 8. All data are within the range of the power-law breakdown. Therefore, the abnormally high stress

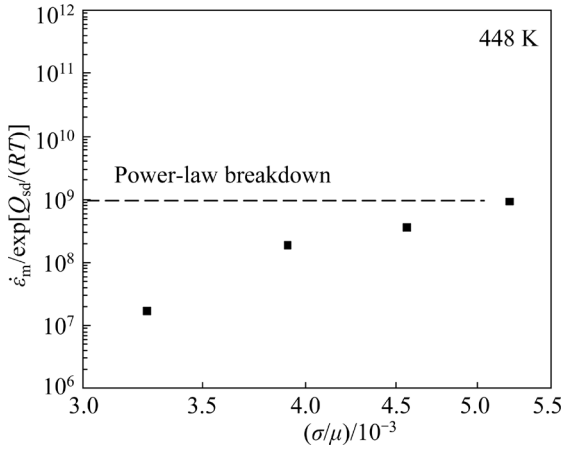

Fig. 8 Plot of steady-state creep rate normalized by activation energy for self-diffusion of Mg against stress normalized by shear modulus

exponent obtained under 448 K and 50−80 MPa conditions is attributed to the dominant role of the alloy power-law breakdown. ZHU et al [17] investigated the creep mechanism of squeeze-cast Mg−Al−Ca alloys in the range of 30−120 MPa and 423−473 K. It was found that there is a high stress exponent that corresponds to a power-law breakdown mechanism.

4 Discussion

4.1 Creep deformation mechanisms

To further elucidate the creep mechanism, TEM observations were performed to examine the microstructural evolution and dislocation patterns. Figures 9 and 10 present typical TEM images of the samples crept at 70 MPa for 50 h, with the corresponding incident beam directions being $\boldsymbol{B}=[\bar{2}110]$.

With the diffraction vector $\boldsymbol{g}=[01\bar{1}0]$, only ⟨*a*⟩ dislocations were detected based on the $\boldsymbol{g}\cdot\boldsymbol{b}=0$ criterion (Fig. 9(a)) [38,39]. The straight lines parallel to the basal plane trace represent the basal ⟨*a*⟩ dislocations, as indicated by the short red arrows. The other short segments perpendicular to the basal plane trace correspond to prismatic ⟨*a*⟩ dislocations [40]. In addition, some kinked or curved dislocation lines (in yellow) are observed, and their angles with respect to $[0002]_{Mg}$ were neither 90° nor 0°, indicating that these line segments may lie in pyramidal planes and/or exist as mixed dislocations [41]. The dark-field image (Fig. 9(b)) clearly shows a significant occurrence of basal ⟨*a*⟩ and prismatic ⟨*a*⟩ slips. With the diffraction vector $\boldsymbol{g}=[0002]$, only ⟨*c*⟩ dislocations are visible, suggesting that the ⟨*c*⟩ dislocations are barely activated (Figs. 8(c, d)). It is evident that the presence of G.P. zones has an inhibitory effect on the prismatic ⟨*a*⟩ slip on pyramidal planes. Hence, for T6-200°C/1h samples, the primary creep mechanism involves the cross-slip of basal ⟨*a*⟩ and prismatic ⟨*a*⟩ dislocations. The G.P. zones are shown to inhibit ⟨*c*⟩ slip. Additionally, in Fig. 9(e), HRTEM images reveal the stable presence of G.P. zones in the T6-200°C/1h sample. There is virtually no precipitation of Al_2Ca during creep deformation. This observation indicates that the G.P. zones consistently maintain a smaller size for their monatomic layer, contributing to the improvement in the creep resistance of the alloy. Therefore, the cross-slip of screw dislocations from the basal plane to the prismatic plane may be the controlling mechanism for the power-law breakdown creep observed in the T6-200°C/1h samples.

The incident beam direction for T6-275°C/8h sample is $\boldsymbol{B}=[\bar{2}110]$. Under $\boldsymbol{g}=[01\bar{1}0]$, a cross-slip containing basal and prismatic dislocation is observed in Fig. 10(b) (indicated by the yellow arrows). The number of cross-slips is higher than that in the T6-200°C/1h sample, indicating that the G.P. zones exert a stronger hindrance to cross-slip than Al_2Ca phases. For the observation under $\boldsymbol{g}=[01\bar{1}0]$, in Figs. 9(a, b), clusters of short slip lines are parallel to basal plane trace. These are basal ⟨*a*⟩ dislocations arranged as dislocation channels (as indicated by the green dotted rectangles), which result from the climbing of dislocations [23]. In Figs. 9(c, e), no obvious ⟨*c*⟩ dislocations are observed. Figure 10(d) shows that a large amount of Al_2Ca phases are uniformly distributed within the grains. During creep deformation, there is an increased quantity of the Al_2Ca phases. Therefore, the creep deformation in the T6-275°C/8h sample is induced by the collective mechanism involving the cross-slip of basal ⟨*a*⟩ and prismatic ⟨*a*⟩ dislocations along with the climb of basal ⟨*a*⟩ dislocations.

4.2 Influence of G.P. zones and Al_2Ca phases on creep properties

Both the T6-200°C/1h and T6-275°C/8h samples exhibit Al−Mn phases. Therefore, the differences in creep properties are primarily determined by the G.P. zones and Al_2Ca phases. In summary, at 175 °C and 50−80 MPa, the creep mechanisms for the T6-200°C/1h and T6-275°C/8h

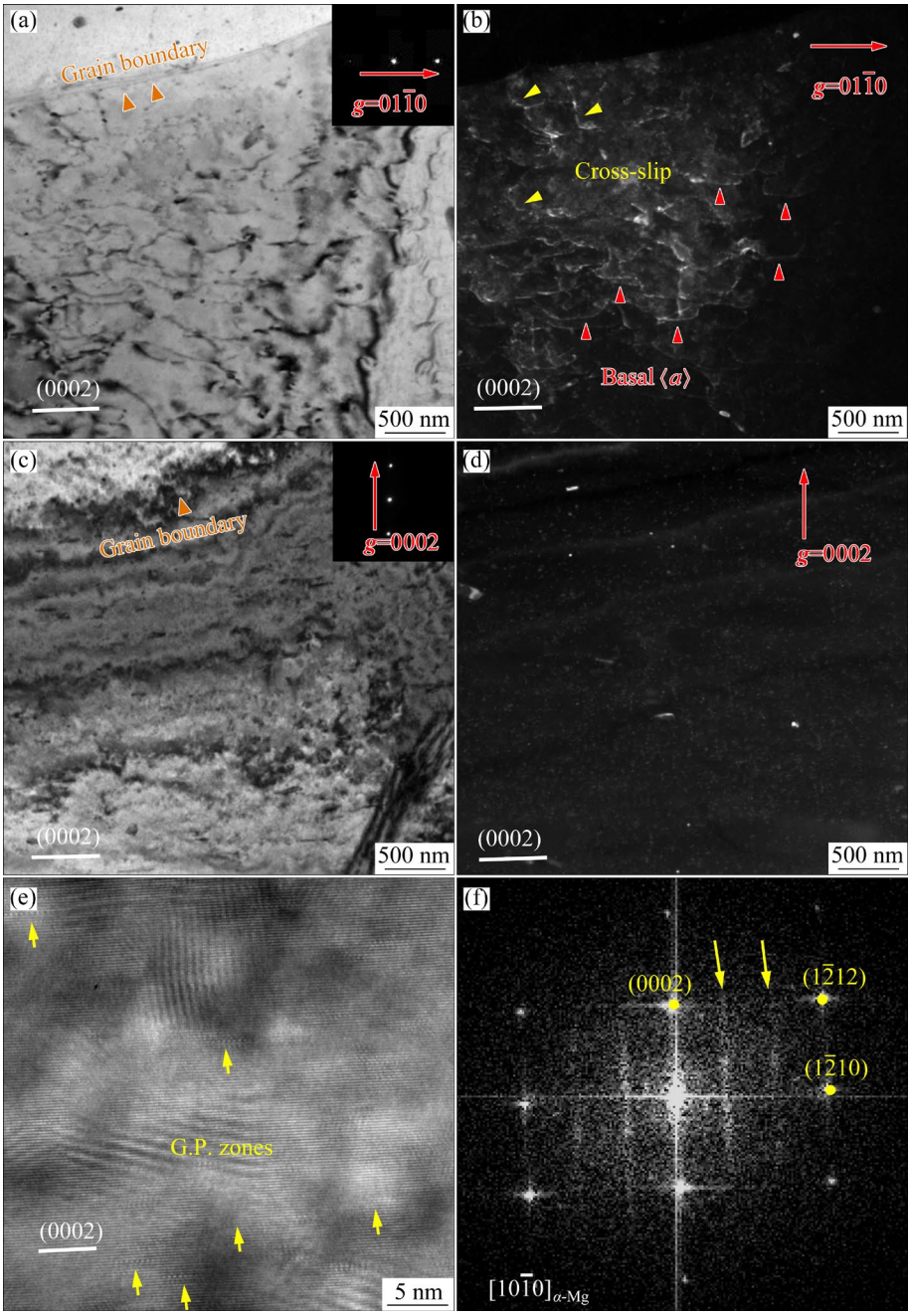

Fig. 9 Bright (a, c) and dark (b, d) field TEM images of T6-200°C/1h sample crept at 70 MPa to 50 h with incident beam direction ***B***=[$\bar{2}$110] and diffraction vectors ***g***= [01$\bar{1}$0] (a, b) and ***g***=[0002] (c, d); HRTEM image (e) and FFT pattern (f) of G.P. zones after creeping

samples differ. The power-law breakdown caused by the cross-slip of screw dislocations from the basal to prismatic plane represents the steady-state creep mechanism in the T6-200°C/1h samples, whereas in the T6-275°C/8h sample, the creep deformation is dominated by both dislocation climbing and cross-slip motion. The presence of G.P. zones and Al_2Ca phases act as effective barriers, hindering the movement of non-basal dislocations.

By comparing the degree of cross-slip observed in Figs. 9(a) and 10(a), it can be concluded that the G.P. zones are more effective on inhibiting dislocation glide and suppressing dislocation climbing. This is also consistent with the observation of ZHANG et al [42] that the ordered G.P. zones can serve as an effective barrier for dislocations to climb and glide during creep deformation. This can be attributed to the higher density of G.P. zones, as shown in Fig. 11 (the number densities of the G.P. zones and the Al_2Ca phases before creep are

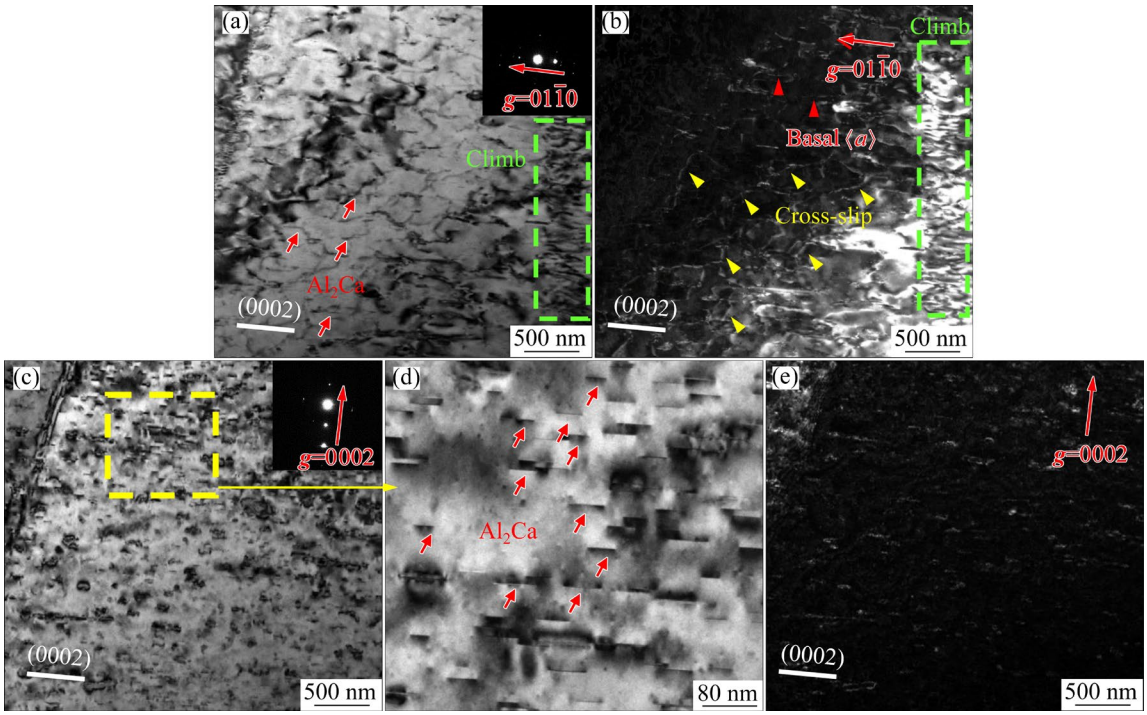

Fig. 10 Bright (a, c, d) and dark (b, e) field TEM images of T6-275°C/8h sample crept at 70 MPa to 50 h with incident beam direction $\boldsymbol{B}$=[$\bar{2}$110] and diffraction vector $\boldsymbol{g}$=[01$\bar{1}$0] (a, b) and $\boldsymbol{g}$=[0002] (c, d, e)

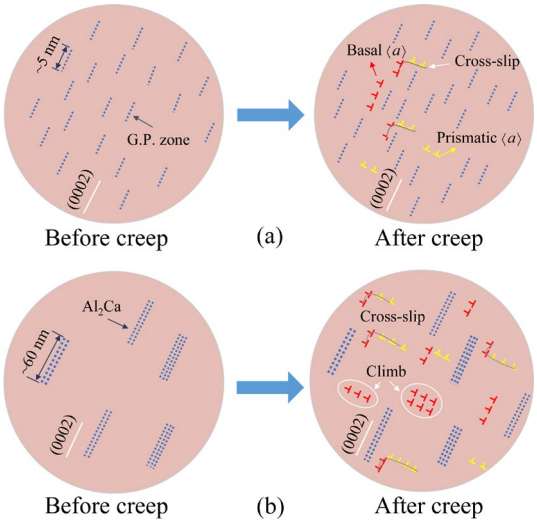

Fig. 11 Schematic diagram of creep mechanism in different samples: (a) T6-200°C/1h; (b) T6-275°C/8h

measured as (1.4±0.3)×10^{23} and (1.2±0.6)×10^{21} m^{-3}, respectively. After creep, the number densities are (2.3±0.2)×10^{23} and (8.1±0.4)×10^{21} m^{-3} for the G.P. zones and the Al$_2$Ca phases, respectively). Furthermore, compared with Al$_2$Ca phases, the G.P. zones maintain a stable monolayer morphology. When precipitates are finer and more uniformly distributed, the average distance of the dislocation glide is reduced, effectively inhibiting dislocation motion and enhancing the creep resistance. Consequently, it is plausible that the creep properties of alloys can be controlled through adjusting the density of high-density G.P. zones. However, obvious dislocations are observed near the Al$_2$Ca phase (Fig. 10). The precipitation of larger Al$_2$Ca phases may induce local structural heterogeneity and introduce stress gradients within the crystals. These gradients can lead to local stress concentrations, particularly at the interfaces between the precipitate and the matrix, serving as a significant driving force for dislocation climbing. Areas with high levels of stress in the local stress field may induce dislocation climbing, allowing the crystal to adapt better to the stress distribution [43]. Conversely, G.P. zones have smaller sizes and a more uniform distribution, which reduces the likelihood of localized stress concentrations and thus hinders the initiation of the dislocation climbing. This phenomenon simultaneously delays the occurrence of creep fractures. However, the interaction between the dislocations and G.P. zone requires further investigation.

5 Conclusions

(1) In addition to Al−Mn phases, the G.P. zones are the dominant precipitates in the T6-200°C/1h

sample, whereas the Al_2Ca phases are the main precipitates in the T6-275°C/8h sample.

(2) The T6-200°C/1h samples exhibit steady-state creep rates ranging from 3.08×10^{-9} s^{-1} to 1.67×10^{-7} s^{-1} in tensile stress range of 50−80 MPa at 175 °C, nearly an order of magnitude lower than the steady-state creep rates of the T6-275°C/8h sample.

(3) The stress exponents for the T6-200°C/1h sample and T6-275°C/8h sample are ~5.5 and ~8.2, respectively. The unusually high stress exponent observed in the T6-200°C/1h sample is associated with the power-law breakdown creep mechanism.

(4) The power-law breakdown creep of the T6-200°C/1h sample is primarily caused by cross-slip of screw dislocations from the basal to prismatic plane, whereas the T6-275°C/8h sample exhibits a collective mechanism involving both dislocation cross-slip and dislocation climb. Compared to the Al_2Ca phases, the dense G.P. zones can effectively inhibit dislocation climb and dislocation glide during creep deformation. Therefore, it is plausible that the creep properties of alloys can be controlled through adjusting the density of high-density G.P. zones.

CRediT authorship contribution statement

Ming-yu LI: Methodology, Validation, Data curation, Writing − Original draft; **Zhi-ping GUAN:** Methodology, Writing − Review & editing; **Jia-wang SONG:** Investigation, Validation, Supervision; **Hong-jie JIA:** Methodology, Investigation; **Pin-kui MA:** Data curation, Methodology; **Gang WANG:** Data collection, Supervision; **Wei YAN:** Experimental data supplement, Investigation; **Ming-hui WANG:** Validation, Supervision; **Zhi-gang LI:** Investigation, Writing − Review & editing.

Declaration of competing interest

The authors declare that they have no known competing financial interests or personal relationships that could have appeared to influence the work reported in this paper.

Data availability statement

The raw/processed data required to reproduce these findings cannot be shared at this time as the data also form part of an ongoing study.

Acknowledgments

This work was supported by the National Natural Science Foundation of China (Nos. 52175322, 52271031), and the Natural Science Foundation of Jilin Province, China (No. SKL202302015).

References

[1] GERASHI E, ALIZADEH R, LANGDON T G. Effect of crystallographic texture and twinning on the corrosion behavior of Mg alloys: A review [J]. Journal of Magnesium and Alloys, 2022, 10: 313−325.

[2] QIU Cheng-liang, LIU Shu-hong, HUANG Jin-hui, DU Yong, YAN Hong, CHEN Rong-shi, HAN En-hou. Phase equilibria and solidification behavior of Mg−Al−Gd casting alloys [J]. Transactions of Nonferrous Metals Society of China, 2024, 34: 1091−1109.

[3] LI Ming-yu, GUAN Zhi-ping, CHEN Peng, REN Ming-wen, WANG Gang, YAN Wei, ZHAO Po, SONG Jia-wang. Anisotropic strain hardening in an extruded lean Mg−Al−Ca−Mn alloy [J]. Materials & Design, 2024, 239: 112770.

[4] WAN Xiao-feng, NI Hong-jun, HUANG Ming-yu, ZHANG Hua-li, SUN Jian-hua. Microstructure, mechanical properties and creep resistance of Mg−(8%−12%)Zn−(2%−6%)Al alloys [J]. Transactions of Nonferrous Metals Society of China, 2013, 23: 896−903.

[5] CHEN Chun-xiang, HUO Qing-huan, ZHANG Zhi-rou, ZHANG Yu-xiu, TANG Jiao, LI Kai-yu, MA Ji-jun, YANG Xu-yue. Effects of precipitate origin and precipitate-free zone development on the tensile creep behaviors of a hot-rolled Mg−13wt.%Gd binary alloy [J]. Materials Characterization, 2021, 178: 111303.

[6] LIU Xi-bo, GUAN Xun, CHEN Rong-shi, HAN En-hou. Creep behavior of ageing hardened Mg−10Gd−3Y alloy [J]. Transactions of Nonferrous Metals Society of China, 2010, 20: s545−s549.

[7] KANG Y H, WANG X X, ZHANG N, YAN H, CHEN R S. Effect of initial temper on the creep behavior of precipitation-hardened WE43 alloy [J]. Materials Science and Engineering A, 2017, 689: 410−426.

[8] CHEN Xin, LI Si-long, WAN Ying-chun. Effect of Gd on preparation of nanocrystalline Mg alloys via cold rotary swaging [J]. Transactions of Nonferrous Metals Society of China, 2024, 34: 1817−1828.

[9] LIU Yu, WANG Na-na, WANG Jin-wei, MA Bai-chang, ZHAO Dong-qing. Investigation of the crystallographic structure and orientations of the Al_2Ca phase in a Mg−Al−Ca−Mn alloy [J]. Materials Characterization, 2018, 142: 377−382.

[10] NAKATA T, XU C, AJIMA R, SHIMIZU K, HANAKI S, SASAKI T T, MA L, HONO K, KAMADO S. Strong and ductile age-hardening Mg−Al−Ca−Mn alloy that can be extruded as fast as aluminum alloys [J]. Acta Materialia, 2017, 130: 261−270.

[11] LI Ming-yu, GUAN Zhi-ping, LIU Li-ping, JIA Hong-jie, LI Zhi-gang, WANG Ming-hui, MA Pin-kui, SONG Jia-wang. Investigation of enhanced strength anisotropy in an extruded Mg−Al−Ca−Mn alloy at cryogenic temperature [J]. Materials Science and Engineering A, 2024, 890: 145940.

[12] ZHANG Lun-yong, WU M, XU Chao, GUO Shu, NING Z L, CAO F Y, HUANG Y J, SUN J F, YI Jun-ying. Creep

behaviors of a Mg−Li based alloy at elevated temperatures [J]. Materials Science and Engineering A, 2021, 827: 142063.

[13] LI Fang, YUAN Ding-ling, CHEN Kang-hua, CHEN Song-yi, LI Li. A novel creep model with synergetic Orowan bypassing and climbing mechanisms in nickel-base superalloys [J]. Transactions of Nonferrous Metals Society of China, 2024, 34: 1167−1177.

[14] BAGHANI A, KHALILPOUR H, MIRESMAEILI S M. Microstructural evolution and creep properties of Mg−4Sn alloys by addition of calcium up to 4 wt.% [J]. Transactions of Nonferrous Metals Society of China, 2020, 30: 896−904.

[15] MO N, MCCARROLL I, TAN Q, CEGUERRA A, LIU Y, CAIRNEY J, DIERINGA H, HUANG Y, JIANG B, PAN F, BERMINGHAM M, ZHANG M X. Understanding solid solution strengthening at elevated temperatures in a creep-resistant Mg−Gd−Ca alloy [J]. Acta Materialia, 2019, 181: 185−199.

[16] LI Z T, ZHANG X D, ZHENG M Y, QIAO X G, WU K, XU C, KAMADO S. Effect of Ca/Al ratio on microstructure and mechanical properties of Mg−Al−Ca−Mn alloys [J]. Materials Science and Engineering A, 2017, 682: 423−432.

[17] ZHU S M, MORDIKE B L, NIE J F. Creep and rupture properties of a squeeze-cast Mg−Al−Ca alloy [J]. Metallurgical and Materials Transactions A, 2006, 37A: 1221−1229.

[18] SUZUKI A, SADDOCK N D, TERMUSH J R, POWELL B R, JONES J W, POLLOCK T M. Precipitation strengthening of a Mg−Al−Ca-Based AXJ530 die-cast alloy [J]. Metallurgical and Materials Transactions A, 2008, 39A: 696−702.

[19] JAYARAJ J, MENDIS C L, OHKUBO T, OH-ISHI K, HONO K. Enhanced precipitation hardening of Mg−Ca alloy by Al addition [J]. Scripta Materialia, 2010, 63: 831−834.

[20] XU S W, OH-ISHI K, KAMADO S, TAKAHASHI H, HOMMA T. Effects of different cooling rates during two casting processes on the microstructures and mechanical properties of extruded Mg−Al−Ca−Mn alloy [J]. Materials Science and Engineering A, 2012, 542: 71−78.

[21] HOMMA T, NAKAWAKI S, KAMADO S. Improvement in creep property of a cast Mg−6Al−3Ca alloy by Mn addition [J]. Scripta Materialia, 2010, 63:1173−1176.

[22] AMBERGER D, EISENLOHR P, GÖKEN M. Microstructural evolution during creep of Ca-containing AZ91 [J]. Materials Science and Engineering A, 2009, 510/511: 398−402.

[23] ZHANG Zhi-rou, HUO Qing-huan, ZHANG Yu-xiu, XIAO Zhen-yu, HASHIMOTO A, YANG Xu-yue. Impacts of artificial aging state on the creep resistance of a rolled Mg−3.5Nd alloy [J]. Materials Science and Engineering A, 2021, 819: 141491.

[24] ZHANG Kai, WANG Cheng, WANG Da-wei, LI Mei-xuan, MA Yin-long, HUA Zhen-ming, ZHANG Lin-yang, LI Jun, WANG Hui-yuan. Effects of solute redistribution during heat treatment on micro-galvanic corrosion behavior of dilute Mg−Al−Ca−Mn alloy [J]. Corrosion Science, 2023, 213: 110971.

[25] ZOU Yan, CAO Ling-fei, WU Xiao-dong, WANG Yi-chang, SUN Xuan, SONG Hui, COUPER M J. Effect of ageing temperature on microstructure, mechanical property and corrosion behavior of aluminum alloy 7085 [J]. Journal of Alloys and Compounds. 2020, 823: 153792.

[26] SONG R G, DIETZEL W, ZHANG B J, LIU W J, TSENG M K, ATRENS A. Stress corrosion cracking and hydrogen embrittlement of an Al−Zn−Mg−Cu alloy [J]. Acta Materialia, 2004, 52: 4727−4743.

[27] OH-ISHI K, WATANABE R, MENDIS C L, HONO K. Age-hardening response of Mg−0.3at.%Ca alloys with different Zn contents [J]. Materials Science and Engineering A, 2009, 526: 177−184.

[28] PING D H, HONO K, NIE J F. Atom probe characterization of plate-like precipitates in a Mg−RE−Zn−Zr casting alloy [J]. Scripta Materialia, 2003, 48: 1017−1022.

[29] CHEN Tao, HU Si-jia, LI Shi-qi, HUO Qing-huan. Uncovering the unexpected changes of creep properties in AZ-series Mg alloys [J]. Materials Science and Engineering: A, 2022, 857: 144056.

[30] ZHANG De-ping, LI Bo-qiong, ZHANG Jin-hui, NIU Ting, LI Chun-lin, CHENG Peng, YANG Liu-qing. Influence of minor RE addition on microstructures, tensile properties, and creep resistance in a die-cast Mg−Al−Ca−Mn alloy [J]. Journal of Materials Research and Technology, 2022, 26: 3136−3145.

[31] WANG Chun-yu, ZHANG Yu-xiu, HUO Qing-huan, ZHANG Zhi-rou, TANG Jiao, HASHIMOTO A, YANG Xu-yue. Effects of twinning time node on the creep properties of dilute Mg−Y alloy [J]. Materials Science and Engineering A, 2021, 800: 140309.

[32] ZHANG Yu-xiu, XIAO Zhen-yu, HUO Qing-huan, ZHANG Zhi-rou, TANG Jiao, HASHIMOTO A, YANG Xu-yue. Effects of pre-compression on the three-dimensional creep anisotropy of a hot-rolled Mg−4wt.%Y binary alloy sheet [J]. Materials Science and Engineering A, 2020, 772: 138843.

[33] XU C, NAKATA T, OH-ISHI K, HOMMA T, OZAKI T, KAMADO S. Improving creep property of Mg−Gd−Zn alloy via trace Ca addition [J]. Scripta Materialia, 2017, 139: 34−38.

[34] SHERBY O D, BURKE P M. Mechanical behavior of crystalline solids at elevated temperature [J]. Progress in Materials Science, 1967, 13: 323−390.

[35] ZHANG Dong-dong, YANG Shuo, MENG Fan-zhi, TIAN Zheng, XU Hong, CAO Zhan-yi, MENG Jian. Compressive creep behavior of extruded Mg−4Sm−2Yb−0.6Zn−0.4Zr alloy [J]. Materials Science and Engineering A, 2021, 809: 140929.

[36] MORDIKE B L. Development of highly creep resistant magnesium alloys [J]. Journal of Materials Processing Technology, 2001, 17: 391−394.

[37] SLUTSKY L J, GARLAND C W. Elastic constants of magnesium from 4.2 K to 300 K [J]. Physical Review, 1957, 107: 972.

[38] DONG X, FENG L, WANG S, JI G, ADDAD A, YANG H, NYBERG E A, JI S. On the exceptional creep resistance in a die-cast Gd-containing Mg alloy with Al addition [J]. Acta Materialia, 2022, 232: 117957.

[39] LI Jia-xiang, HUO Qing-huan, WANG Chun-yu, ZHANG Yu-xiu, ZHANG Zhi-rou, FENG Gang, YANG Xu-yue. Tension-compression asymmetry in hot-rolled Mg−3wt%Gd alloy under creep loading [J]. Materials Science and Engineering A, 2022, 831: 142124.

[40] MO N, MCCARROLL I, TAN Q, CEGUERRA A, CAIRNEY J, DIERINGA H, HUANG Y, JIANG B, PAN F, BERMINGHAM M, ZHANG M X. Roles of Nd and Mn in a new creep-resistant magnesium alloy [J]. Materials Science and Engineering A, 2020, 779: 139152.

[41] YANG Biao-biao, WANG Jun, Ferdowsi Mahmoud Reza Ghandehari, CHAO Qi, GAO Xiang, LI Yun-ping, ZHU Yu-man, Barnett Matthew, LLorca Javier. Effect of precipitates on the dominant active slip systems in Mg−4.5Zn(wt.%) alloy [J]. Acta Materialia, 2024, 278: 120231.

[42] ZHANG De-ping, ZHANG Jin-hui, XU Tao, ZHANG Ya-qin, CHE Chao-jie, ZHANG Dong-dong, MENG Jian. Significant improvement in creep property of a Mg−Yb based alloy via introducing nano-spaced stacking faults [J]. Materials Science and Engineering A, 2020, 845: 143238.

[43] ZHANG Yu-xiu, XIAO Zhen-yu, HUO Qing-huan, LUO Lu, LI Kai-yu, HASHIMOTO Aki, YANG Xu-yue. Effects of initial texture on the three-dimensional creep anisotropic behaviors of dilute Mg−Y binary alloy sheets [J]. Materials Science and Engineering A, 2019, 766: 138336.

不同人工时效处理对挤压低含量 Mg−Al−Ca−Mn 合金拉伸蠕变行为的影响

李明宇[1]，管志平[1]，宋家旺[1]，贾红杰[1]，马品奎[1]，王 刚[2]，闫 巍[2]，王明辉[1]，李志刚[1]

1. 吉林大学 材料科学与工程学院 汽车材料教育部重点实验室，长春 130022；
2. 一汽模具制造有限公司，长春 130000

摘 要：探讨了人工时效(T6)对挤压 Mg−1.22Al−0.31Ca−0.44Mn(质量分数，%)合金在 175 ℃、50~80 MPa 拉应力作用下的蠕变性能的影响。在 200 ℃时效 1 h (T6-200℃/1h)的样品中，主要析出 Guinier-Preston (G.P.)区，而在 275 ℃时效 8 h(T6-275℃/8h)的样品中，主要析出相为 Al_2Ca。T6-200℃/1h 样品表现出优异的抗蠕变性能，其稳态蠕变速率比 T6-275℃/8h 样品的低一个数量级。T6-200℃/1h 样品中观察到的异常高应力指数(~8.2)与幂律失效机制相关。经透射电子显微镜(TEM)分析发现，T6-200℃/1h 样品的蠕变机制由基面和柱面位错之间的交滑移主导，而 T6-275℃/8h 样品表现出位错交滑移和攀移的混合机制。与 Al_2Ca 相相比，密集的 G.P.区在蠕变过程中能有效阻碍位错的攀移和滑移，T6-200℃/8h 样品表现出更优异的抗蠕变性能。

关键词：Mg−Al−Ca−Mn 合金；拉伸蠕变；人工时效；交滑移

(Edited by Bing YANG)